JACS
JOURNAL OF THE AMERICAN CHEMICAL SOCIETY
Article
pubs.acs.org/JACS

Helical Ribbons for Molecular Electronics

Yu Zhong,[‡] Bharat Kumar,[‡] Seokjoon Oh,[‡] M. Tuan Trinh,[‡] Ying Wu,[‡] Katherine Elbert,[‡] Panpan Li,[†] Xiaoyang Zhu,[‡] Shengxiong Xiao,*[,†] Fay Ng,*[,‡] Michael L. Steigerwald,*[,‡] and Colin Nuckolls*[,†,‡]

[†] Department of Chemistry, Optoelectronic Nano Materials and Devices Institute, Shanghai Normal University, Shanghai, China
[‡]Department of Chemistry, Columbia University, New York, New York 10027, United States

Supporting Information

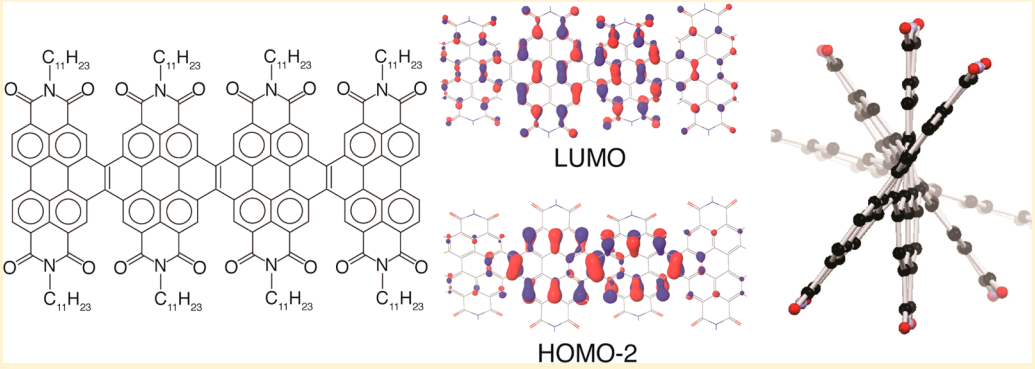

ABSTRACT: We describe the design and synthesis of a new graphene ribbon architecture that consists of perylenediimide (PDI) subunits fused together by ethylene bridges. We created a prototype series of oligomers consisting of the dimer, trimer, and tetramer. The steric congestion at the fusion point between the PDI units creates helical junctions, and longer oligomers form helical ribbons. Thin films of these oligomers form the active layer in n-type field effect transistors. UV−vis spectroscopy reveals the emergence of an intense long-wavelength transition in the tetramer. From DFT calculations, we find that the HOMO−2 to LUMO transition is isoenergetic with the HOMO to LUMO transition in the tetramer. We probe these transitions directly using femtosecond transient absorption spectroscopy. The HOMO−2 to LUMO transition electronically connects the PDI subunits with the ethylene bridges, and its energy depends on the length of the oligomer.

INTRODUCTION

This manuscript describes the design, synthesis and electrical characterization of electron deficient graphene nanoribbons. Graphene, the atomically thin two-dimensional crystal of graphite, has an unusual set of qualities that make it useful for both fundamental research[1−3] and numerous applications.[4−6] However, graphene is limited for many electronic applications because it is a zero-band gap semiconductor. It was predicted that narrow nanoribbons exhibit different electronic states.[7] In order to open a sufficient electronic gap, narrow graphene nanoribbons with sub-10 nm widths are required to yield acceptable on/off transistor operation at room temperature.[8−10] There are several top-down methods to create thin graphene ribbons,[11−17] but the usefulness of the resulting ribbons is limited by the width not being atomically defined and the functional groups on the edge being uncontrolled.[13] A number of bottom-up approaches to synthesize graphene nanoribbons also exist.[18−22] The bottom-up approach is advantageous because it provides an atomically precise synthesis of nanoribbons without any structural defects. It also gives access to chemical modification along the edges to tune solubility, electrical characteristics, and conformation of the ribbons. Müllen and co-workers have reported several methods for synthesis of graphene nanoribbons either in solution[19,20,22] or on metal surfaces.[21] Despite these studies, there is a dearth of methods to produce n-type, electron transporting ribbons.[18] The present study fills that void by providing a synthetic method to make atomically defined graphene nanoribbons comprising perylene-3,4,9,10-tetracarboxylic acid diimide (PDI, **1** in Figure 1) subunits bridged with C═C subunits. We describe a new synthetic procedure to fuse PDIs together with an ethylene bridge forming dimer **2**, trimer **3**, and tetramer **4** (Figure 1). The physical and electronic structure of this series of oligomers is a consequence of the unusual fusion in the ribbon backbone. The steric congestion introduced by the fusion between the PDIs causes the ribbons to become severely contorted into helical superstructures.

The PDI core has been heavily investigated as a chromophore and as an n-type organic semiconductor. The PDI subunit has found many applications in field effect transistors (FETs),[23] light-emitting diodes (LEDs),[24] and organic photovoltaics (OPVs).[25,26] PDI is a versatile building block for the synthesis of graphene nanoribbons because many synthetic routes have been developed to functionalize the bay positions of the aromatic

Received: April 9, 2014
Published: May 20, 2014

   dx.doi.org/10.1021/ja503533y | J. Am. Chem. Soc. 2014, 136, 8122−8130

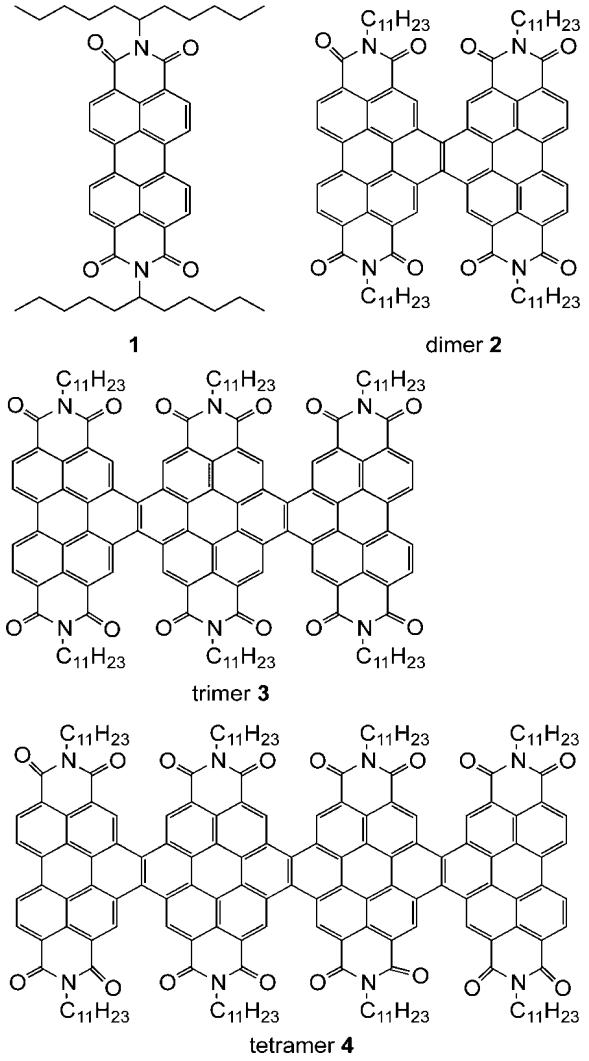

Figure 1. PDI monomer **1**, dimer **2**, trimer **3**, and tetramer **4**.

core.[25,27−29] Pi-conjugated oligomers with PDI units have been reported.[18,30] Notably, Wang and co-workers have prepared graphene nanoribbons with a zigzag fusion of PDI building blocks by means of a copper-mediated coupling of a tetrachloro-substituted PDI.[18] However, their approach suffers from low yields and the lack of structural control for the synthesis of higher oligomers. The dimer **2** was synthesized recently from a step-intensive synthesis in an overall yield that is less than 1%.[30] Here we describe a new strategy to synthesize n-type graphene nanoribbons from PDI subunits. Our approach gives the precise control over the final structure and can be extended to the synthesis of higher oligomers.

RESULTS AND DISCUSSION

Oligomer Synthesis. Scheme 1 summarizes the synthesis of the dimer **2**. Experimental details are contained in the Supporting Information. We couple *trans*-1,2-bis(tributylstannyl)ethene (**5**) to the monobromo-PDI (**6**)[31] via a Stille coupling in 88% yield.[27] We then oxidatively cyclized the ethylene-bridged PDI **9** using Mallory photocyclization.[32,33] Optimum conditions for the photocyclization to **2** required both I_2 and purging with air under irradiation with a 450 W Hanovia medium pressure mercury lamp. Under these conditions high yields (~83%) could be obtained for the dimer **2**.

We also found a method to create the important PDI monostannane building block **8**, shown in Scheme 1. This building block is essential for the higher oligomer syntheses. We show two alternative syntheses of the trimeric PDI **3** in Scheme 2. Coupling monostannane **8** with either the monobrominated dimer **10**, in Scheme 2A (see the Supporting Information for synthesis of **10**) or with the dibrominated parent PDI[34] (**7**, in Scheme 2B) furnishes the substrates for the photocyclization. Again we applied the Mallory conditions developed for the dimer; both substrates yield the trimer **3** in >60% yield. The yield of **3** (from **11** or **12**) is in actuality much higher, but it is difficult to chromatograph the cyclized PDI oligomers due to their tendency to bind to the silica during chromatography.

Two analogous routes were developed for the tetrameric PDI **4** shown in Scheme 3. In Scheme 3A we couple the monobrominated dimer **10** with 1,2-bis(tributylstannyl)ethene (**5**) to yield **13**. In Scheme 3B, we couple monostannane **8** with the dibrominated dimer **14** (see the Supporting Information for synthesis of **14**).[35] Each of these substrates produced the tetramer **4** upon photocyclization. It is perhaps ironic that the

Scheme 1. Synthesis of Dimer 2[a]

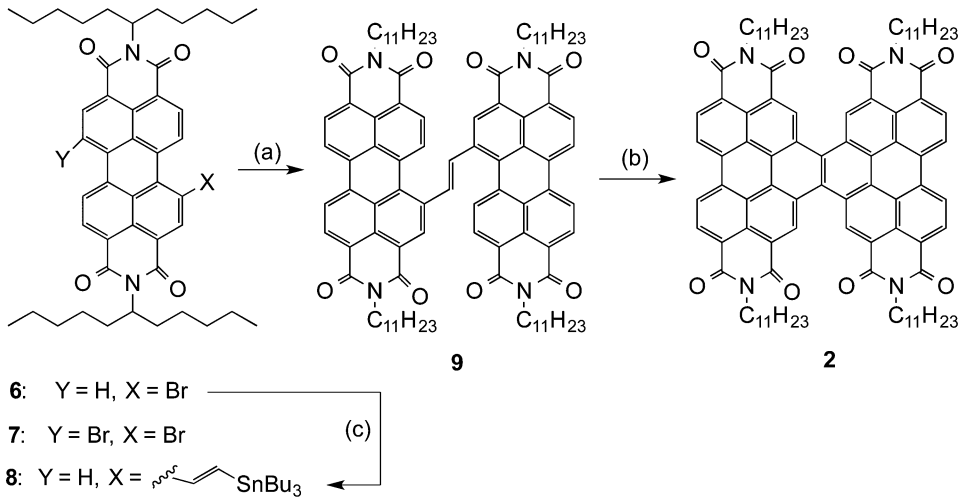

[a]Key: (a) **5**, $Pd(PPh_3)_4$, PhMe, reflux, 88%; (b) I_2, air, $h\nu$, PhH, 83%; (c) **5**, $Pd(PPh_3)_4$, PhMe, reflux, 70%.

dx.doi.org/10.1021/ja503533y | J. Am. Chem. Soc. 2014, 136, 8122−8130

Scheme 2. Synthesis of Trimeric PDI 3[a]

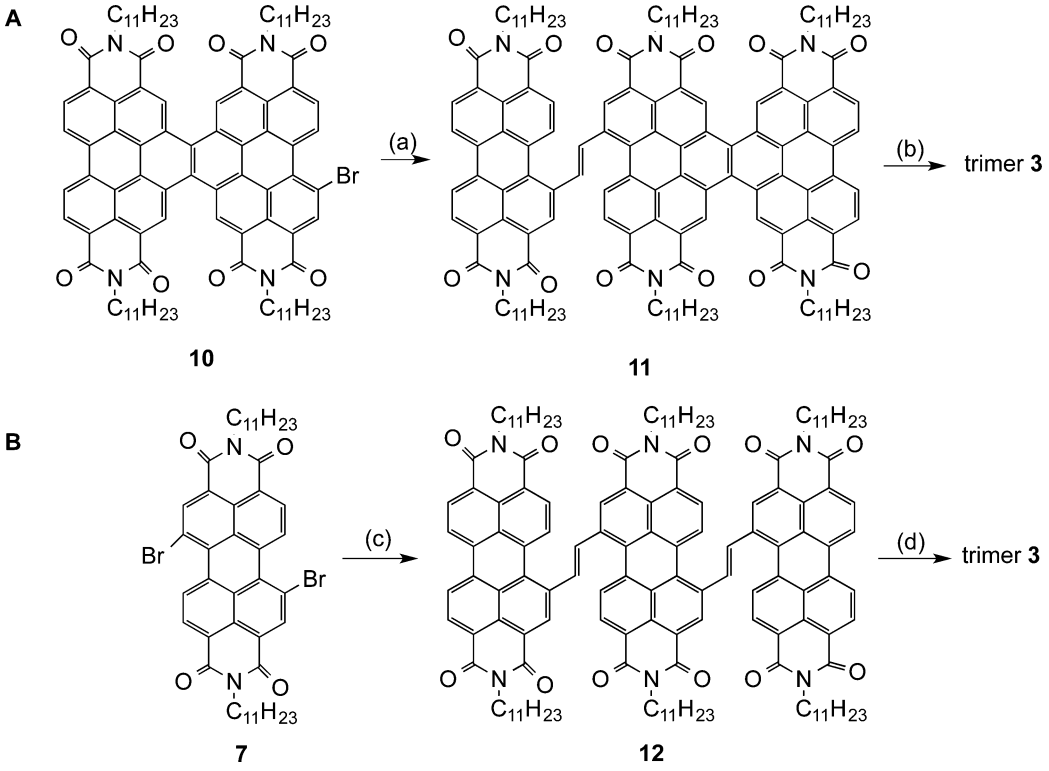

[a]Key: (a) **8**, $Pd(PPh_3)_4$, PhMe, reflux, 93%; (b) I_2, air, $h\nu$, PhMe, 63%; (c) **8**, $Pd(PPh_3)_4$, PhMe, reflux, 47%; (d) I_2, air, $h\nu$, PhMe, 62%

Scheme 3. Synthesis of the Tetrameric PDI 4[a]

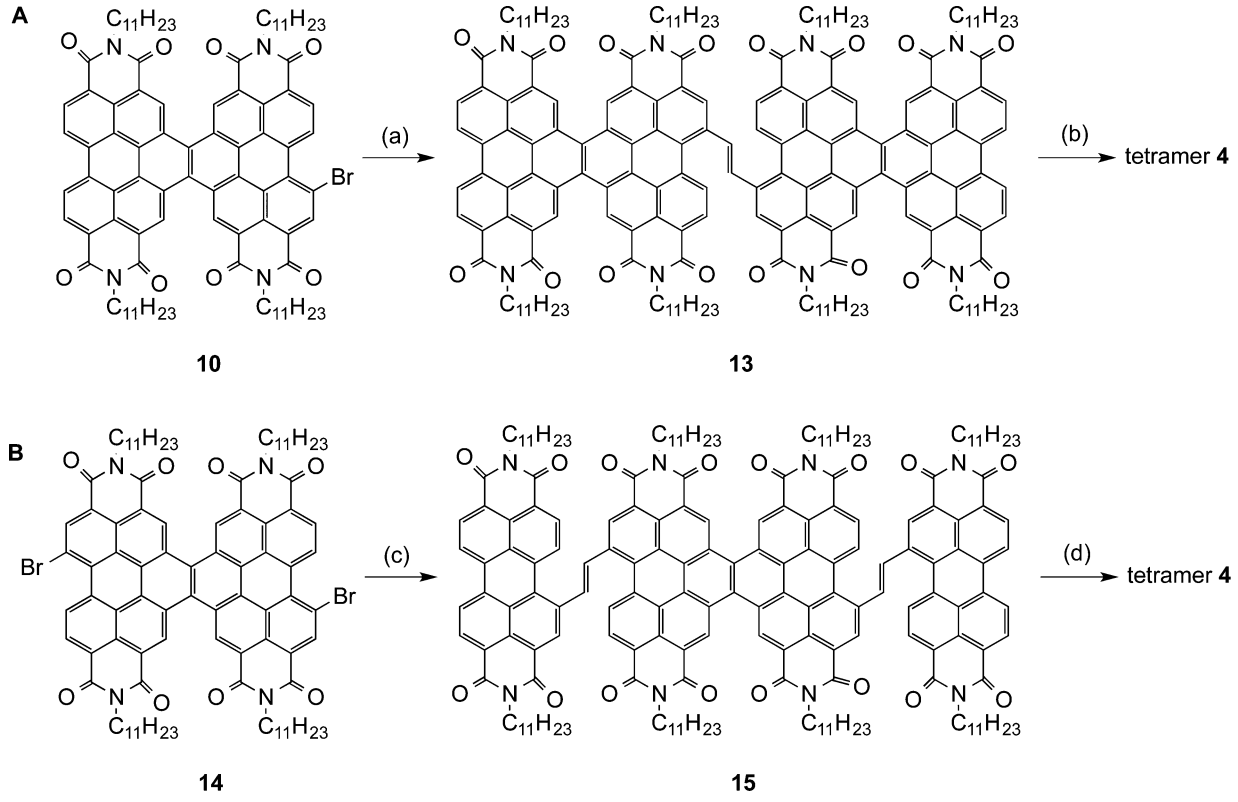

[a]Key: (a) **5**, $Pd(PPh_3)_4$, PhMe, reflux, 65%; (b) I_2, air, $h\nu$, PhMe; (c) **8**, $Pd(PPh_3)_4$, PhMe, reflux, 72%; (d) I_2, air, $h\nu$, PhMe, 45%.

reaction mixture resulting from the double photocyclization in Figure 3B was much cleaner than that resulting from the apparently intimately related single photocyclization in Scheme 3A. The mixture in Scheme 3A contains partially cyclized

dx.doi.org/10.1021/ja503533y | J. Am. Chem. Soc. 2014, 136, 8122−8130

products that are difficult to separate from the desired product. Therefore, we synthesize the tetramer according to Scheme 3B. Given the high yields, the solubility of the products, and the generality of this method, it is likely that this method can yield substantially longer oligomers.

All oligomers (from dimer to tetramer) are isolated as dark red solids having a metallic sheen. The oligomers are soluble in common organic solvents including toluene, chloroform and dichloromethane. They are insoluble in methanol and ethanol. One advantage of a nonplanar core is that it maintains its solubility and processability for the longer oligomers. The oligomers are thermally robust; TGA (see the Supporting Information) does not show any detectable decomposition below 400 °C. The oligomers are also resistant to oxidation as evident by absence of any oxidation peak in CV up to +1 V in Bu_4NPF_6 solution (0.1 M) as the electrolyte in dichloromethane (vide infra).

Conformation of the Ribbons. We have been unable to grow single crystals of these materials of sufficient quality for X-ray structure determination, so we relied on DFT optimized structures to gain insight into molecular conformations of the oligomers. To simplify the calculations, we replaced the $C_{11}H_{23}$ side chain attached to each nitrogen atom with a single H. The influence of alkyl N-substituents on the electronic structures is negligible due to the nodes of frontier orbitals at the imide nitrogens.[36,37] The nonplanar conformation of the ribbons is a consequence of repulsion between the two C−H bonds on the inner bay position of adjacent PDI units. This steric repulsion causes them to twist away from planarity. This can be seen clearly for the model of the dimer shown in Figure 2A. The dimer has a helical twist along ribbon axis meaning that the dimer exists as mixture of enantiomers.[30] (The Supporting Information contains the atomic coordinates from the DFT calculations.) We performed variable temperature ^{1}H NMR (between −5 to 100 °C) to determine if there was conformational interchange on the NMR time scale; however, the only detectable dynamics for

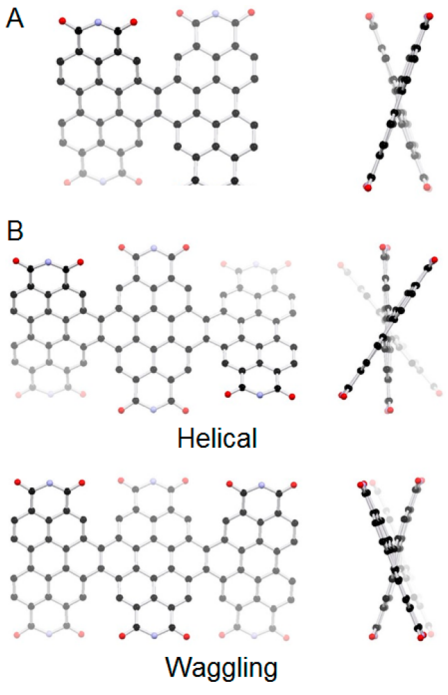

Figure 2. DFT models of (A) dimer **2** and (B) trimer **3**.

2, **3**, or **4** were due to the hindered rotation of the amide N−CHR bond (Figure S8−S10).[31,34] The broadening of the ^{1}H NMR resonances due to these rotational isomers obscure details about which conformer exists at room temperature.

The trimer structure consists of two conformational options (Figure 2B). When the helicity at each of the fusion points has the same handedness, the ribbon is helical. The pitch of this helix is 7.0 nm/turn. We call this the "Helical" conformation in Figure 2B. If the helical sense in the first junction between PDIs is opposite to that of the second junction, then the ribbon is achiral. We call this the "Waggling" conformation in Figure 2B.

DFT calculations reveal that the tetramer **4** has three possible conformers. Two of these conformations are directly analogous to those from the trimer, the helical and waggling conformers (Figure 3). Now having three ring junctions, the tetramer can

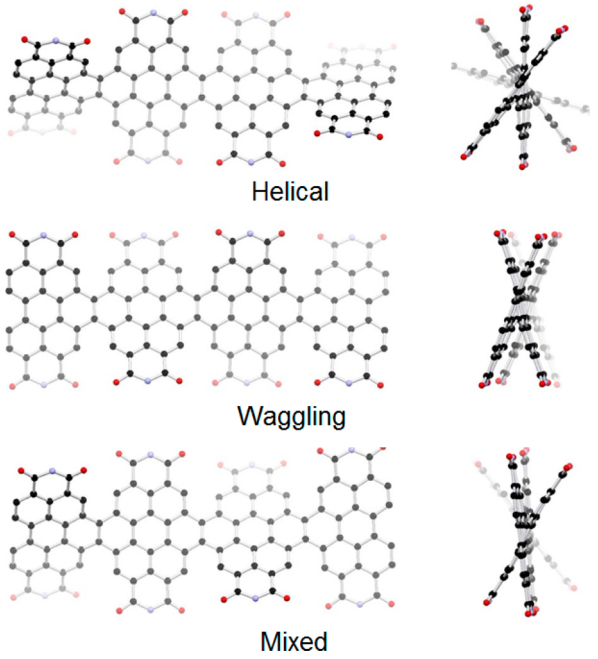

Figure 3. DFT models of tetramer **4**.

adopt a conformation that is a mixture of helical and waggling. We refer to this as the "Mixed" conformer. We calculated the relative energies of each of the conformers, and for both the trimer and tetramer all of the competing conformations are isoenergetic.

Electrical Measurements. Electrochemical measurements in CH_2Cl_2 with Bu_4NPF_6 (0.1 M) as the supporting electrolyte reveal that **2**−**4** can accept electrons (Figure S5).[38] The trimer **3** and tetramer **4** can accept up to five electrons. From the potential of the first reduction peak, the LUMO was estimated to be −3.77, −3.82, and −3.84 eV for **2**, **3**, and **4**, respectively. These values are slightly lower than the LUMO level of PDI monomer[18,30] and close to that of common n-type materials such as [6,6]-phenyl-C_{61}-butyric acid methyl ester ($PC_{60}BM$).[39,40]

We constructed field-effect transistors (FETs) using **2**, **3**, and **4** as the semiconductor to compare their ability to transport electrons. We first treat the substrate (300 nm of SiO_2 on a Si wafer) with octadecyltrichlorosilane (OTS) in order to passivate traps on the SiO_2 surface.[41,42] We then spin-cast films of **2**, **3**, and **4** onto this surface. The thickness of the organic films is 15−20 nm. Transistors made from thicker films (40−60 nm) exhibit nonlinear characteristic at low bias voltage. Au source and drain

dx.doi.org/10.1021/ja503533y | J. Am. Chem. Soc. 2014, 136, 8122−8130

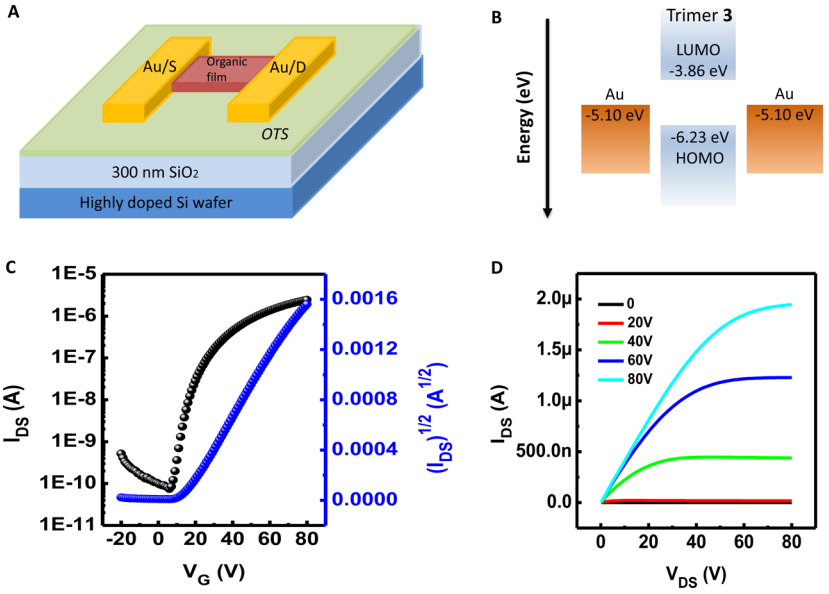

Figure 4. (A) Schematic of a FET device structure. (B) Energy diagram for Au/trimer **3**/Au. (C) Transfer and (D) output characteristics of FET for **3**.

electrodes are deposited on the film to make a bottom-gate and top-contact configuration with $W = 105\ \mu m$ and $L = 15\ \mu m$. The schematic of the FET device structure is shown in Figure 4A along with the corresponding energy level diagram (Figure 4B). The samples were annealed (under inert atmosphere) to optimize device performance. All of the oligomers form n-type, electron-transporting semiconductors. The typical transfer and output curves for **3** are shown in Figure 4C,D. The FET characteristics for **2** and **4** are similar to those of **3** (see Table 1);

Table 1. FET Performance of 2, 3, and 4

	mobility[a]/cm^2 V^{-1} s^{-1}	log(I_{on}/I_{off})	V_{th}/V
2	0.02[b]	~6	11
3	0.04[c]	~5	10
4	0.05[d]	~5	8

[a]Measured in nitrogen-filled glovebox. [b]Annealed at 160 °C for 10 min. [c]Annealed at 240 °C for 10 min. [d]Annealed at 200 °C for 10 min. Annealing temperatures reported here are the optimal annealing conditions for the corresponding materials.

Figure S6 contains the IV curves for **2** and **4**. The mobility was calculated in the saturation regime[43,44] using $I_{DS} = (W/2L)\ C_i\mu(V_G - V_T)^2$, where W and L are the width and length of the channel, C_i (11.5 nFcm^{-2}), μ, and V_T correspond to the capacitance per unit area of the gate insulator, the field effect mobility, and the threshold voltage, respectively. The mobility increases from dimer **2** to tetramer **4**. The FETs for compound **4** exhibits the highest electron mobility, 0.05 cm^2 V^{-1} s^{-1}. The average threshold voltage varies from 11 to 8 V.[45−48]

The previously reported mobility for PDI monomers with similar structure to **1** range from 0.1 to 2 cm^2 V^{-1} s^{-1}.[46−49] PDIs featuring planar structure show strong self-aggregation, which facilitates intermolecular charge carrier transport.[47,48] Here, all of the compounds **2**−**4** formed very smooth films as evident from their AFM images (Figure S7) with RMS of 0.32, 0.34, and 0.27 nm, respectively. No significant crystalline grains were observed. This is probably due to the twisted structures of **2**−**4** that reduces long-range crystallinity.

Electronic Structure. We show the absorption and emission spectra for **1** through **4** in Figure 5. Comparison of these spectra through the series raised several questions we sought to answer. The first is simple: what is the source of the shift to the red of the lowest energy excitation? The second is less well-defined: while the series of absorptions in the monomer has been assigned to a vibrational progression,[50,54] the spectra of **2**, **3**, and **4** do not appear as simple, are other higher-energy absorptions present in

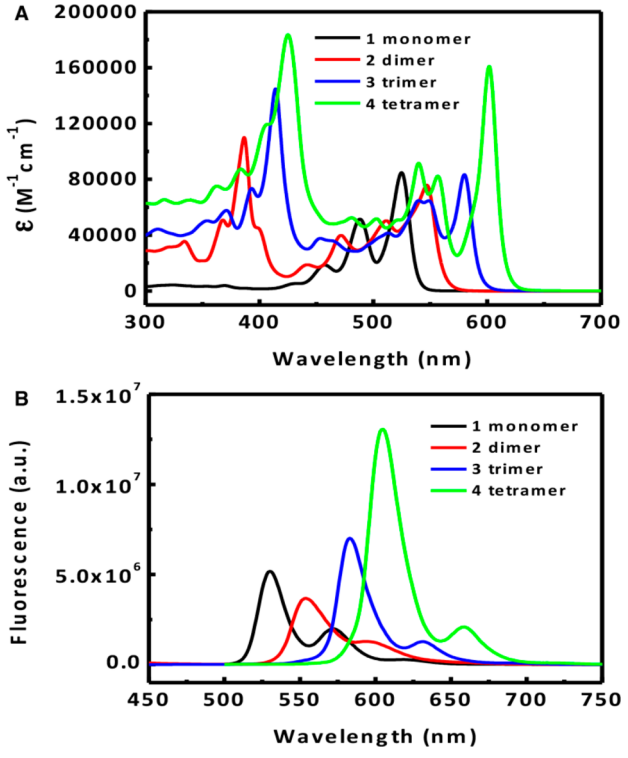

Figure 5. (A) UV−vis absorption spectra of monomer **1**, dimer **2**, trimer **3**, and tetramer **4** (1×10^{-5} M concentration in dichloromethane with a path length $l = 1$ cm). (B) Fluorescence spectra of **1** excited at 488 nm, **2** excited at 386 nm, **3** excited at 414 nm, and **4** excited at 425 nm (1×10^{-7} M in dichloromethane).

dx.doi.org/10.1021/ja503533y | J. Am. Chem. Soc. 2014, 136, 8122−8130

addition to (or in place of) any vibrational signatures? The third question focuses on the tetramer; why is its lowest-energy absorption so intense? The fourth question is more evident: what is the source of the shorter-wavelength absorptions (~350 to ~450 nm) that show up in the oligomers but are absent in the monomer?

The calculated physical structures of **1**–**4** show that we may idealize the PDI-oligomers as individually flat PDI units that are linked by contorted C═C moieties. (In each case the C–C–C–C dihedral angle around the C═C subunits that link the PDI subunits is roughly 155°.) One of our goals was to determine how these subunits interact to yield the electronic behavior of the ultimate nanoribbon. We performed quantum chemical (ground-state DFT and excited state TD-DFT) calculations on the PDI oligomers to better understand these effects and answer the question posed above. We show the computed absorption spectra for **1**–**4** as Figures S11–S17 in the Supporting Information.

In Table 2 we compare the optical HOMO–LUMO gap with the computed HOMO–LUMO gap for **1**–**4.** In each molecule the HOMO is formed primarily from the C–C π orbitals arrayed in alternating phase around the central six-membered rings (Figure 6A),[51] and in each molecule the LUMO may be viewed as a similar combination of the corresponding C–C π^* orbitals (Figure 6B). Excited-state (TD-DFT) calculations show that in the monomer, dimer, and trimer the lowest-energy electronic excitation moves one electron from the HOMO to the LUMO. The energy of this HOMO–LUMO excitation decreases with increasing oligomer length due to quantum confinement similar to that seen in conjugated molecules or semiconductor clusters.[18,52,53] We also note that the calculated absorption spectrum for **1** is quite simple, showing only a single peak in the visible region; this is in agreement with the previous assignment of the set of equally spaced absorptions as a vibrational progression.[54] Therefore, our first question above has a simple answer (at least in elementary, single-electron terms): the lowest-energy optical absorption effectively moves one electron from the HOMO to the LUMO, and as one moves from **1** to **4** both the HOMO and LUMO energies are lowered, but that of the LUMO lowers faster.

Table 2. Computational and Optical Data for 1, 2, 3, and 4

	computational[a]			optical[b]	
	E_{HOMO}/eV	E_{LUMO}/eV	E_{gap}/eV	λ_{max}/nm	E_{gap}/eV
1	−6.11	−3.58	2.53	525	2.36
2	−6.19	−3.77	2.41	547	2.27
3	−6.23	−3.86	2.37	580	2.14
4	−6.26	−3.91	2.35	602	2.06

[a]Calculations were performed at the B3LYP/6-31G** level. [b]Optical band gaps were estimated from the wavelength of the absorption peak.

While the calculated absorption spectrum of **1** is very simple, the spectra of **2**, **3**, and **4** are more complex. For example, while the calculated spectrum of **1** shows only one peak for wavelengths longer than 350 nm, that of **2** shows at least five and that of **3** at least seven. These facts, along with the definite nonplanarity of the oligomers, suggest an answer to our second question above: that their higher-energy absorptions are not due exclusively to vibronic effects. Further, according to our TD-DFT calculations in **2** and **3**, the second-lowest-energy allowed transition promotes an electron from the HOMO−2 to the LUMO. In each case the HOMO−2 is the highest-energy

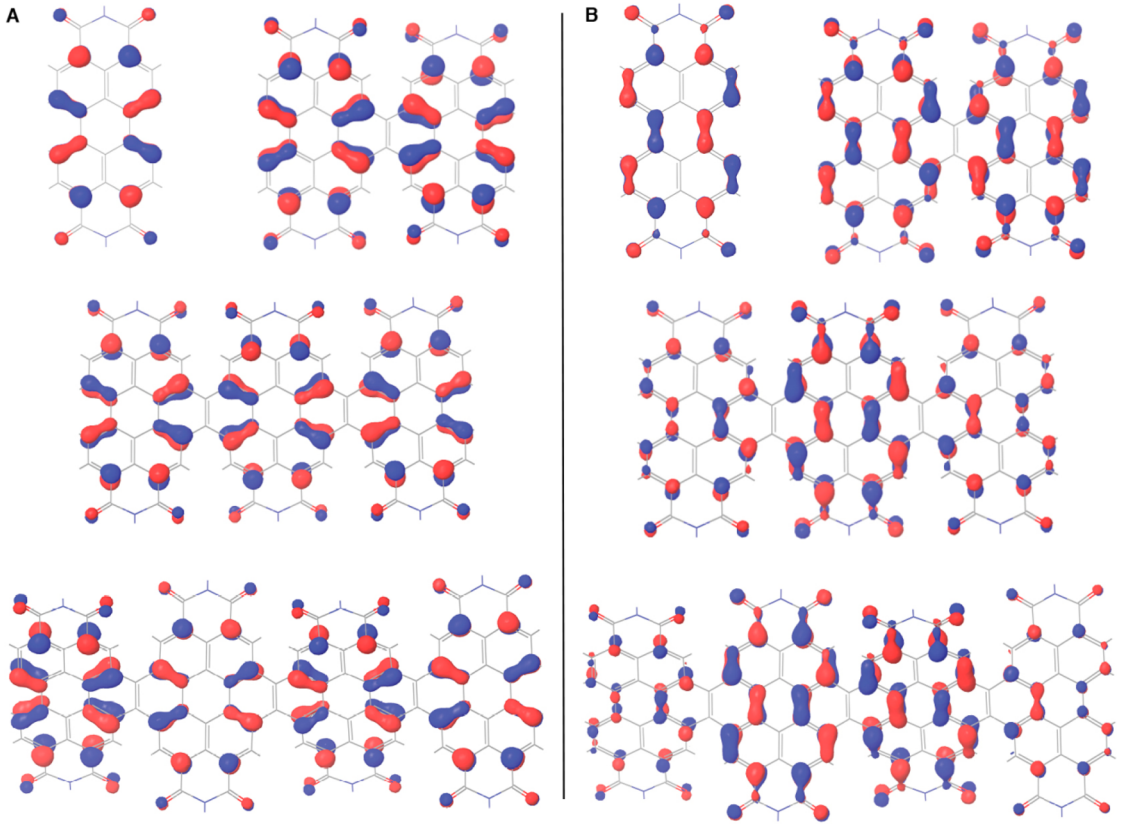

Figure 6. (A) Highest occupied molecular orbitals for PDI oligomers. (B) Lowest unoccupied molecular orbitals of PDI oligomers.

dx.doi.org/10.1021/ja503533y | J. Am. Chem. Soc. 2014, 136, 8122–8130

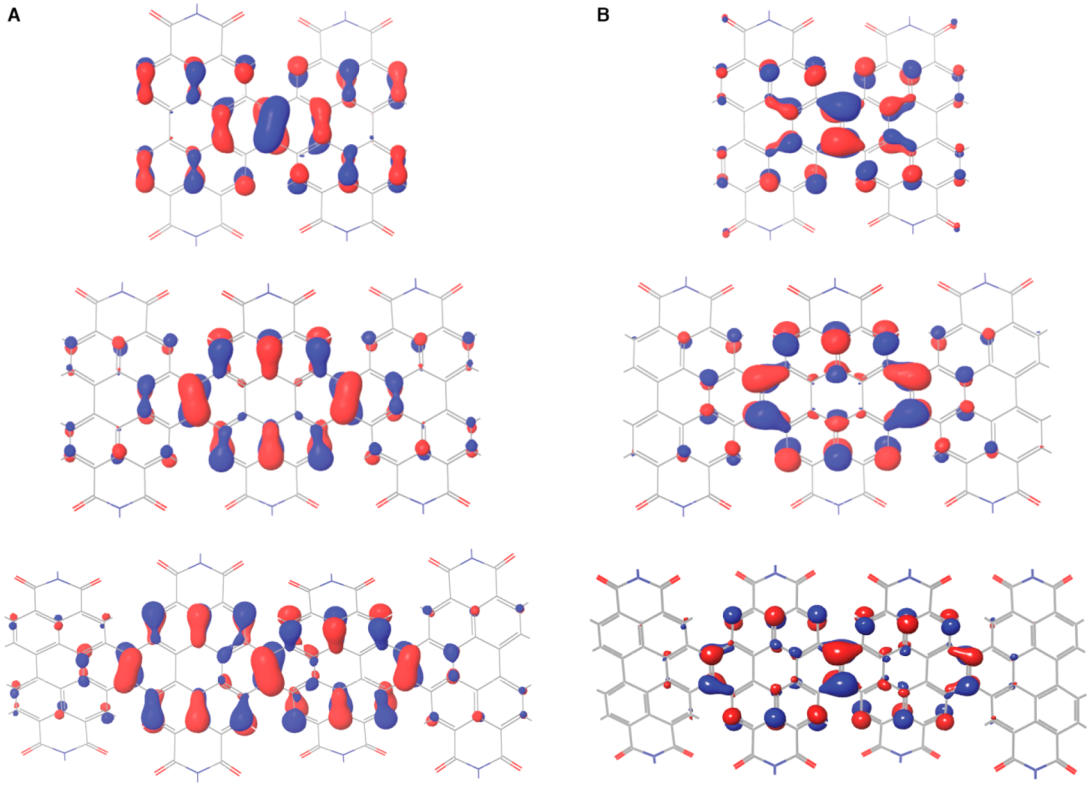

Figure 7. (A) HOMO−2 for PDI oligomers. (B) Lowest energy antibonding orbital of the bridging olefin.

occupied orbital that can be associated with C═C bonds that bridge the PDI units. Since the LUMO in each molecule is associated with the PDI subunits, we view this (HOMO−2)-to-LUMO transition as promoting an electron from the bridging C═C subunit array to the PDI subunit array. As with the HOMO−LUMO transition, this excitation also shifts to lower energy with increasing oligomer size. The shift of this (HOMO−2)-to-LUMO to increasingly lower energy with degree of oligomerization is also the source of the very intense longest-wavelength absorption in **4** (Figure 5A). This (HOMO−2)-to-LUMO transition also answers our third question above: it is important to note that the energy of this transition in the tetramer is calculated to be essentially the same as that of the HOMO-to-LUMO transition. In fact, the calculated oscillator strength for the (HOMO−2)-to-LUMO transition is much larger than that of the HOMO−LUMO transition. The energy of the HOMO−2 is only slightly lower (~4 mh = ~0.1 eV) than that of the HOMO, so the C═C and PDI subunits are close to degenerate in the tetramer; this hints that the longer oligomers will provide an even richer photophysics. Our calculations on **2**, **3**, and **4** show a third important type of electronic transition. In these, an electron is promoted from the molecular HOMO (situated primarily on the PDI subunits) to an orbital that is best characterized as a π^* orbital of the bridging olefin (Figure 7B). This transition is quite strong and occurs at higher energies. This type of transition accounts for the families of shorter-wavelength absorptions in the oligomers and answers the fourth of the questions we posed above.

To probe these transitions directly we use femtosecond transient absorption spectroscopy; the technique was described elsewhere.[55] We excite the sample of **4** with a 450 nm laser pulse and probe with a white light supercontinuum. Figure 8 shows transient absorption spectra as a function of probe photon energy

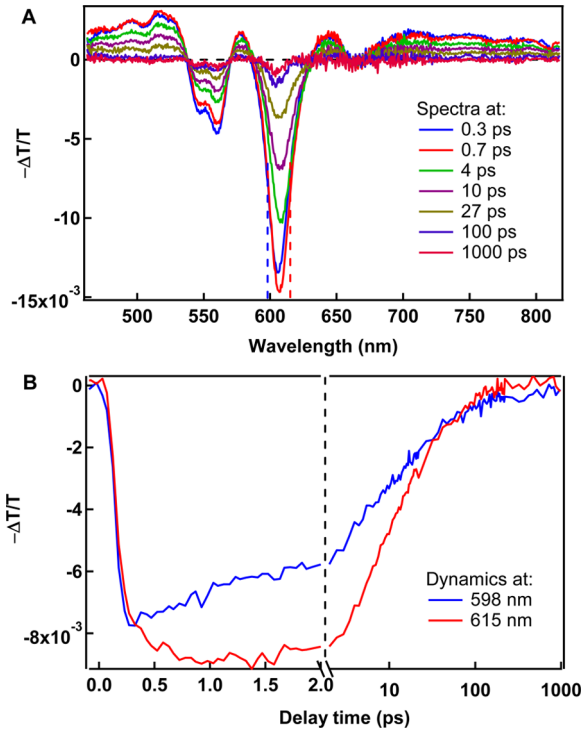

Figure 8. (A) Different transmission, $-\Delta T/T$, as a function of probe photon energy at different delay time between pump and probe pulses. (B) Exciton dynamics probing at the red side (615 nm) and blue side (598 nm) of the absorption peak at 605 nm (red and blue dashed lines in panel A).

for **4** at different delay times between pump and probe pulses. The negative signals at 550 and 605 nm are due to photo

dx.doi.org/10.1021/ja503533y | J. Am. Chem. Soc. 2014, 136, 8122−8130

bleaching from the absorption peaks at the same wavelengths. The positive signals are due to photoinduced absorption in the transitions from S_1 to higher lying singlet states. The bleaching peaks are spectrally better resolved than corresponding features in the static spectrum. In particularly, the bleaching features at 605 and 550 nm are well separated; this confirms that the absorption at 550 nm is not vibrational progression associated with the transition centered at 605 nm. Figure 8B presents the dynamics at the red side (615 nm) and the blue side (598 nm) of the absorption peak centered at 605 nm. It is clear that the dynamics are very different. These dynamics can be fitted well by a biexponential function. While the decay constants for the dynamics at 598 nm are 2.5 and 28 ps, the dynamics at 615 nm are 8 and 48 ps. This result is in line with the DFT calculation in which the lowest-energy allowed transition is combination of the (HOMO−2)-to-LUMO and the HOMO-to-LUMO transitions in the tetramer. According to the calculation the difference in energy for these two transitions is ∼0.1 eV. We note that the bleaching dynamics for **1** are similar at different probe wavelengths. The Supporting Information contains a comparison of the transient absorption spectra for **1**, **2**, and **4** and the dynamics for **1** at different probe wavelengths. This transient absorption data experimentally answers the above questions 2 and 3.

Therefore, we can at least partially assign the optical spectra (Figure 5) by citing three families of electronic transition. The first is the HOMO−LUMO transition, and it is roughly similar in the monomer, dimer, trimer, and tetramer. These transitions involve orbitals confined to the PDI subunits; there is little orbital density on the bridging olefins. Only the monomer shows a vibrational progression.[54] In the higher oligomers that are distorted away from planarity, the vibronic effects are absent. In the second family of optical transitions, an electron is promoted from a C=C bonding level in the bridging olefin(s) (Figure 7A) to the LUMO. Since the LUMO is situated on the PDI subunits, this transition is from the olefinic bridges to the PDI framework. These transitions are slightly higher in energy than the HOMO−LUMO transitions in the dimer and trimer, but in the tetramer the two transitions are essentially degenerate. The third family of transitions promotes an electron from the HOMO to antibonding levels of the bridging olefins. Since the HOMO is situated on the PDI subunits, this transition is from the PDI framework to the olefinic bridges. These transitions are all higher in energy, accounting for the shorter wavelength absorptions we see in the dimer, trimer, and tetramer spectra (Figure 5).

CONCLUSION

In summary, we report here synthesis of a new series of n-type graphene nanoribbons based on PDI oligomers. As the ribbons increase in size their band gaps narrow, and in consequence they show a red-shift of their absorption edge relative to that of the PDI monomer. Their photophysical behavior and electronic structure suggests a bifurcation into PDI and bridging olefin subsystems, and these subsystem merge energetically in the longer oligomers, giving rise to intense, long-wavelength absorbances. Their strong absorption in the 400 to 600 nm range forms a complement to the absorption spectra of low-band gap electron donor polymers typically used in solar cells. The newly synthesized oligomers are good electron acceptors and form n-type field effect film transistors. Taken, together, the optical, electronic, and charge-transport properties of the oligomers show that they are promising candidates for the OLED and photovoltaic applications.[25,56,57]

ASSOCIATED CONTENT

Supporting Information

Synthetic details, TGA data, UV−vis spectra, cylic voltammograms, transfer and output curves of TFTs, AFM images, ^{1}H and ^{13}C NMR spectra, VT-NMR spectra, computational details, and transient absorption spectra. This material is available free of charge via the Internet at http://pubs.acs.org.

AUTHOR INFORMATION

Corresponding Author

senksong@msn.com; fwn2@columbia.edu; mls2064@columbia.edu; cn37@columbia.edu

Notes

The authors declare no competing financial interest.

ACKNOWLEDGMENTS

This work was supported as part of the program "Center for Re-Defining Photovoltaic Efficiency Through Molecule Scale Control", an Energy Frontier Research Center funded by the U.S. Department of Energy, Office of Science, Office of Basic Energy Sciences under Award Number DE-SC0001085, with additional support from the Shanghai Municipal Science and Technology Commission (No. 12nm0504000). S.X. thanks the Program for Professor of Special Appointment (Eastern Scholar) at Shanghai Institutions of Higher Learning (No.2013-57), and Program for Changjiang Scholars and Innovative Research Team in University (PCSIRT, IRT1269). M.T.T. and X.Y.Z. were supported by Department of Energy under Grant No. ER46673 DE-SC0001928.

REFERENCES

(1) Novoselov, K. S.; Geim, A. K.; Morozov, S. V.; Jiang, D.; Zhang, Y.; Dubonos, S. V.; Grigorieva, I. V.; Firsov, A. A. *Science* **2004**, *306*, 666.

(2) Novoselov, K. S.; Geim, A. K.; Morozov, S. V.; Jiang, D.; Katsnelson, M. I.; Grigorieva, I. V.; Dubonos, S. V.; Firsov, A. A. *Nature* **2005**, *438*, 197.

(3) Zhang, Y. B.; Tan, Y. W.; Stormer, H. L.; Kim, P. *Nature* **2005**, *438*, 201.

(4) Eda, G.; Fanchini, G.; Chhowalla, M. *Nat. Nanotechnol.* **2008**, *3*, 270.

(5) Bunch, J. S.; van der Zande, A. M.; Verbridge, S. S.; Frank, I. W.; Tanenbaum, D. M.; Parpia, J. M.; Craighead, H. G.; McEuen, P. L. *Science* **2007**, *315*, 490.

(6) Chung, K.; Lee, C. H.; Yi, G. C. *Science* **2010**, *330*, 655.

(7) Fujita, M.; Wakabayashi, K.; Nakada, K.; Kusakabe, K. *J. Phys. Soc. Jpn.* **1996**, *65*, 1920.

(8) Son, Y.-W.; Cohen, M. L.; Louie, S. G. *Phys. Rev. Lett.* **2006**, *97*, 216803.

(9) Barone, V.; Hod, O.; Scuseria, G. E. *Nano Lett.* **2006**, *6*, 2748.

(10) Wang, X.; Ouyang, Y.; Li, X.; Wang, H.; Guo, J.; Dai, H. *Phys. Rev. Lett.* **2008**, *100*, 206803.

(11) Top-down approach includes chemical or plasma etching graphene sheets, laterally unzipping carbon nanotubes (CNTs), patterning graphene by nanowire mask and direct growth of graphitic nanoribbon from a DNA template. See refs 12−17.

(12) Li, X.; Wang, X.; Zhang, L.; Lee, S.; Dai, H. *Science* **2008**, *319*, 1229.

(13) Wei, D. C.; Xie, L. F.; Lee, K. K.; Hu, Z. B.; Tan, S. H.; Chen, W.; Sow, C. H.; Chen, K. Q.; Liu, Y. Q.; Wee, A. T. S. *Nat. Commun.* **2013**, *4*, 1374.

(14) Xie, L.; Jiao, L.; Dai, H. *J. Am. Chem. Soc.* **2010**, *132*, 14751.

(15) Jiao, L.; Zhang, L.; Wang, X.; Diankov, G.; Dai, H. *Nature* **2009**, *458*, 877.

(16) Bai, J. W.; Duan, X. F.; Huang, Y. *Nano Lett.* **2009**, *9*, 2083.

(17) Sokolov, A. N.; Yap, F. L.; Liu, N.; Kim, K.; Ci, L.; Johnson, O. B.; Wang, H.; Vosgueritchian, M.; Koh, A. L.; Chen, J.; Park, J.; Bao, Z. *Nat. Commun.* **2013**, *4*, 2402.
(18) Qian, H. L.; Negri, F.; Wang, C. R.; Wang, Z. H. *J. Am. Chem. Soc.* **2008**, *130*, 17970.
(19) Yang, X.; Dou, X.; Rouhanipour, A.; Zhi, L.; Räder, H. J.; Müllen, K. *J. Am. Chem. Soc.* **2008**, *130*, 4216.
(20) Fogel, Y.; Zhi, L. J.; Rouhanipour, A.; Andrienko, D.; Rader, H. J.; Mullen, K. *Macromolecules* **2009**, *42*, 6878.
(21) Cai, J.; Ruffieux, P.; Jaafar, R.; Bieri, M.; Braun, T.; Blankenburg, S.; Muoth, M.; Seitsonen, A. P.; Saleh, M.; Feng, X.; Müllen, K.; Fasel, R. *Nature* **2010**, *466*, 470.
(22) Schwab, M. G.; Narita, A.; Hernandez, Y.; Balandina, T.; Mali, K. S.; De Feyter, S.; Feng, X. L.; Mullen, K. *J. Am. Chem. Soc.* **2012**, *134*, 18169.
(23) Anthony, J. E.; Facchetti, A.; Heeney, M.; Marder, S. R.; Zhan, X. W. *Adv. Mater.* **2010**, *22*, 3876.
(24) Ego, C.; Marsitzky, D.; Becker, S.; Zhang, J.; Grimsdale, A.; Müllen, K.; MacKenzie, J.; Silva, C.; Friend, R. *J. Am. Chem. Soc.* **2003**, *125*, 437.
(25) Zhou, E. J.; Cong, J. Z.; Wei, Q. S.; Tajima, K.; Yang, C. H.; Hashimoto, K. *Angew. Chem., Int. Ed.* **2011**, *50*, 2799.
(26) Sharenko, A.; Proctor, C. M.; van der Poll, T. S.; Henson, Z. B.; Nguyen, T.-Q.; Bazan, G. C. *Adv. Mater.* **2013**, *25*, 4403.
(27) Huo, L. J.; Zhou, Y.; Li, Y. F. *Macromol. Rapid Commun.* **2008**, *29*, 1444.
(28) Yan, Q. F.; Zhao, D. H. *Org. Lett.* **2009**, *11*, 3426.
(29) Li, C.; Wonneberger, H. *Adv. Mater.* **2012**, *24*, 613.
(30) Li, Y.; Wang, C.; Li, C.; Di Motta, S.; Negri, F.; Wang, Z. *Org. Lett.* **2012**, *14*, 5278.
(31) Schmidt, C. D.; Lang, N.; Jux, N.; Hirsch, A. *Chem.—Eur. J.* **2011**, *17*, 5289.
(32) Mallory, F. B.; Mallory, C. W. In *Organic Reactions*; John Wiley & Sons, Inc.: Hoboken, NJ, 1984; Vol. *30*.
(33) Mallory, C. W. M. F. B. *Org. Photochem. Synth.* **1971**, *1*, 55.
(34) Rajasingh, P.; Cohen, R.; Shirman, E.; Shimon, L. J. W.; Rybtchinski, B. *J. Org. Chem.* **2007**, *72*, 5973.
(35) Dibrominated dimer **14** was synthesized by electrophilic bromination of dimer **2**, and the mixture was used without separation as both isomers (1,6 or 1,7) will give same product.
(36) Sang Kwon, L.; Yanbing, Z.; Andreas, H.; Yves, G.; Kläus, M.; Allen, J. B. *J. Am. Chem. Soc.* **1999**, *121*, 3513.
(37) Wurthner, F. *Chem. Commun.* **2004**, 1564.
(38) Details of the electrochemical measurements can be found in the Supporting Information, Figure S5.
(39) He, Y.; Li, Y. *Phys. Chem. Chem. Phys.* **2011**, *13*, 1970.
(40) Yan, Z.; Yunlong, G.; Yunqi, L. *Adv. Mater.* **2013**, *25*, 5372.
(41) Rozlosnik, N.; Gerstenberg, M. C.; Larsen, N. B. *Langmuir* **2003**, *19*, 1182.
(42) Chua, L.-L.; Zaumseil, J.; Chang, J.-F.; Ou, E. C. W.; Ho, P. K. H.; Sirringhaus, H.; Friend, R. H. *Nature* **2005**, *434*, 194.
(43) Zaumseil, J.; Sirringhaus, H. *Chem. Rev.* **2007**, *107*, 1296.
(44) Newman, C. R.; Frisbie, C. D.; da Silva, D. A.; Bredas, J. L.; Ewbank, P. C.; Mann, K. R. *Chem. Mater.* **2004**, *16*, 4436.
(45) The threshold voltages are in the similar range of reported PDI transistors. See refs 46−48.
(46) Chesterfield, R. J.; McKeen, J. C.; Newman, C. R.; Ewbank, P. C.; da Silva, D. A.; Bredas, J. L.; Miller, L. L.; Mann, K. R.; Frisbie, C. D. *J. Phys. Chem. B* **2004**, *108*, 19281.
(47) Chen, F. C.; Liao, C. H. *Appl. Phys. Lett.* **2008**, *93*, 103310.
(48) Tatemichi, S.; Ichikawa, M.; Koyama, T.; Taniguchi, Y. *Appl. Phys. Lett.* **2006**, *89*, 112108.
(49) Malenfant, P. R. L.; Dimitrakopoulos, C. D.; Gelorme, J. D.; Kosbar, L. L.; Graham, T. O.; Curioni, A.; Andreoni, W. *Appl. Phys. Lett.* **2002**, *80*, 2517.
(50) Türkmen, G.; Erten-Ela, S.; Icli, S. *Dyes Pigm.* **2009**, *83*, 297.
(51) Xiao, S.; Myers, M.; Miao, Q.; Sanaur, S.; Pang, K.; Steigerwald, M. L.; Nuckolls, C. *Angew. Chem., Int. Ed.* **2005**, *44*, 7390.
(52) Nolde, F.; Pisula, W.; Müller, S.; Kohl, C.; Müllen, K. *Chem. Mater.* **2006**, *18*, 3715.
(53) Steigerwald, M. L.; Alivisatos, A. P.; Gibson, J. M.; Harris, T. D.; Kortan, R.; Muller, A. J.; Thayer, A. M.; Duncan, T. M.; Douglass, D. C.; Brus, L. E. *J. Am. Chem. Soc.* **1988**, *110*, 3046.
(54) Sadrai, M.; Bird, G. R. *Opt. Commun.* **1984**, *51*, 62.
(55) Trinh, M. T.; Sfeir, M. Y.; Choi, J. J.; Owen, J. S.; Zhu, X.-Y. *Nano Lett.* **2013**, *13*, 6091.
(56) Zhang, X.; Lu, Z.; Ye, L.; Zhan, C.; Hou, J.; Zhang, S.; Jiang, B.; Zhao, Y.; Huang, J.; Zhang, S.; Liu, Y.; Shi, Q.; Liu, Y.; Yao, J. *Adv. Mater.* **2013**, *25*, 5791.
(57) Yan, Q.; Zhou, Y.; Zheng, Y.-Q.; Pei, J.; Zhao, D. *Chem. Sci.* **2013**, *4*, 4389.